Ultrabroad acoustical limiting in nonlinear metamaterials due to adaptive-broadening band-gap effect

Xin Fang,[1,*] Jihong Wen,[1,†] Henri Benisty,[2] and Dianlong Yu[1]

[1]*Laboratory of Science and Technology on Integrated Logistics Support, College of Intelligent Science and Technology, National University of Defense Technology, Changsha, Hunan 410073, China*

[2]*Université Paris-Saclay, Institut d'Optique Graduate School, CNRS, Laboratoire Charles Fabry, 91127, Palaiseau, France*

(Received 26 January 2019; revised manuscript received 18 February 2020; accepted 20 February 2020; published 4 March 2020)

Nonlinear wave limiters transmit low-amplitude waves while blocking high-intensity ones for efficient target protection. However, the acoustical limiting effect in nonlinear materials remains hitherto unaddressed. In addition, tunable bandgap fosters advanced functions for devices, but it is still mostly regarded as a spatial and temporal invariant feature. In recent years, nonlinear acoustic metamaterials (NAM) have shown extraordinary properties for manipulating elastic waves. Here we achieve an enhanced nonlinear interaction in a different NAM. We theoretically and experimentally demonstrate that the NAM features an efficient acoustical limiting, and the limiting bandwidth adaptively broadens as the propagation distance/time increases. Within a short propagation distance, an ultrabroad limiting band is formed that overcomes the limitation of linear resonant bandgaps. It is clarified that the space-amplitude-dependent bandgap dominates the amplitude reduction, and the transient chaotic responses initialize the adaptive-broadening process. Our study highlights wave physics that could not obviously be realized in nonlinear optics. The self-adaptive band structures open up opportunities to realize exotic adaptive elements.

DOI: 10.1103/PhysRevB.101.104304

I. INTRODUCTION

Major technological revolutions in recent decays have been based primarily on our improved ability to manipulate sound, heat, light, and electrons [1–3]. A plethora of sensitive elements for agile devices, including diodes, amplifiers, switches, and limiters, are made of nonlinear materials [4]. The nonlinear optical limiting allows the transmitting of low-level light while blocking high-intensity pulses [5,6]. It has been successfully used for protecting sensors and eyes from lasers in wide swaths of engineering [7]. The limiting effect can be generated through nonlinear refraction/ scattering, reverse saturable absorption, free-carrier absorption, and two-photon/multiphoton absorption [8]. Recently, optical limiters are realized with nonlinear photonic crystals and metamaterials [9,10], and broad bandwidth is desired [11]. Actually, it is well known that nonlinearity can limit the resonant amplitudes. Phonons are responsible for the transmission of sound, vibration, and heat in our everyday life. They cover an extremely broad spectrum from 1 Hz to 1THz [12]. Acoustical limiters, if there are, cannot only usefully protect us from high-intensity elastic/acoustic waves, but also offer new ways for controlling noise, vibration, and heat. However, acoustical limiting in nonlinear elastic/acoustic materials has not been clearly established yet, to the best of our knowledge.

Moreover, advanced functions can be realized by tuning the crystal bands [13–15]. For linear monocrystals or metamaterials, evanescent waves in bandgaps decay exponentially as the propagation distance [16], but the attenuation bandwidth keeps unchanged. Therefore, bandgaps of linear crystals can only be tuned by altering the material or structural parameters [17]. The essential reason has been indicated by Bloch theorem: linear band structure is space-time invariant. Bandgaps of nonlinear crystals are amplitude-dependent for both light and sound [18–22]. However, it was still regarded as invariable for specified amplitude, though it is generally described as tunable with variable amplitude. As is well known, many self-actions have been reported in nonlinear optics and acoustics [5,23], like self-focusing, self- trapping, and self-phase modulation. Those self-actions depend on the propagation distance and time in materials. However, it is still quite unclear if the band-gap width can be adaptive.

At last, low-frequency and broad bandgaps are desired in extensive applications [24,25]. Acoustic metamaterials [26–28] (AMs) offer unusual functions in manipulating low-frequency elastic waves [29,30]. However, obtaining broad locally resonant (LR) bandgaps whose generalized width $\gamma > 1$ (i.e., over an octave, see Appendix) remains a great challenge [31] due to the limitation of the mass ratio [32]. Nonlinear AMs (NAMs) [19,33,34] can boost the exploration of features such as nonreciprocity [35,36], harmonic generation [37], broadband chaotic passbands [38,39] and bridging coupling [40]. Most recently, Fang *et al.* realized the ultralow-frequency and ultrabroad band (double-ultra) wave attenuation in finite NAMs [38,39] based on the chaotic passband [39]. Bridging

*xinfangdr@sina.com
†wenjihong@vip.sina.com

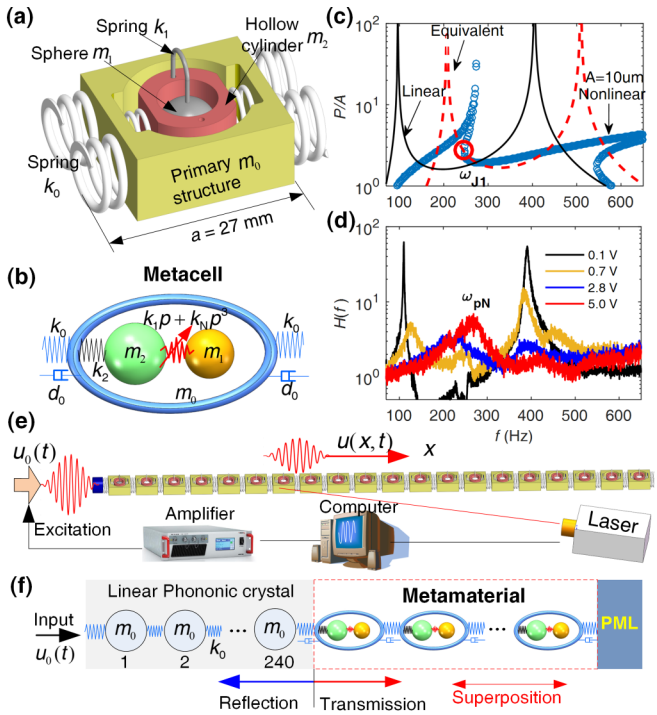

FIG. 1. Prototype. (a) Experimental metacell. (b) Triatomic metacell. (c) Transmission of local resonances, i.e., the value P/A solved with Eq. (4), where curves of nonlinear model (i.e., the dark blue circles) are calculated with $k_N = 1 \times 10^{13}\,\mathrm{N/m^3}$, $A = 10\,\mu\mathrm{m}$ The big red circle is the bifurcation point. The dashed red curve is the equivalent linear result. (d) Experimentally measured transmission of a single cell by driving m_0 with white-noise signals. The voltage, V, gives the exciter amplitude. The result for 0.1 V denotes the linear state. (e) Experimental NAM chain consists of 30 metacells (only 20 cells are shown here). (f) Numerical NAM model.

coupling of nonlinear LR bandgaps offers an efficient way for manipulating chaotic passbands [40]. However, adaptive properties in NAM have not been well understood. One key challenge lies in fabricating a metamaterial whose nonlinearity is strong enough to generate a large bandgap shifting with achievable amplitudes in general experiments.

Here, we report a NAM with enhanced nonlinear interactions. We present the first theoretical and experimental demonstration of both the acoustical limiting and adaptive-broadening band-gap effects. The band structure and bandgap self-adapt to the propagation distance/time, which induces an efficient ultralow-frequency and ultrabroad (double-ultra) acoustical limiting. The limiting band overcomes the bandwidth limitation that depends on the mass ratio. The mechanisms for initializing the adaptive-broadening are elucidated. We state that this work is essentially different from previous work on the chaotic band [38,39].

II. MODELS AND METHODS

Unusual phenomena occur in a NAM containing strongly coupled resonators featuring enhanced nonlinearity. A typical NAM prototype that we fabricated to evidence this is shown in Fig. 1. In the metacell, the primary oscillator m_0 is a hollowed parallelepiped, and two neighboring m_0 units are coupled through a pair of springs whose entire stiffness is k_0. The hollow cylinder m_2 held inside m_0 has a hole whose radius is 4.045 mm. m_2 couples to m_0 by two springs with total stiffness k_2. A steel sphere m_1 is held at the center point of the cylindroid cavity in m_2, and the two are connected by a curved spring whose stiffness is k_1. There is a symmetrical clearance, $\delta_0 = 45 \pm 15\,\mu$m, between the sphere and the cylinder wall at rest. Specifying $p(t)$ as the relative displacement between m_1 and m_2, a strongly nonlinear interaction happens if $|p(t)| > \delta_0$ because m_1 collides with m_2 in this case. Therefore, m_1 and m_2 are vibroimpact oscillators [41], and the force between them, $F_N(t)$, is a piecewise-defined function. The tiny clearance, δ_0, is paramount to generating enhanced nonlinearity. The NAM prototype consists of 30 metacells with lattice constant $a = 27$ mm. The prototype is put on a guide rail and m_0 contacts the sliding rail surface. Its left terminal is connected to a vibration exciter through k_0, and the other end is fixed [Fig. 1(e)]. More experimental images are provided in Ref. [42].

If only the first linear resonances of m_0, m_1, and m_2 in the x direction are considered, the entire metacell is equivalent to the triatomic configuration shown in Fig. 1(b). The motion equations for the n^{th} cell are

$$\begin{aligned} m_0\ddot{u}_n &= k_0(u_{n+1} + u_{n-1} - 2u_n) \\ &\quad + d_0k_0(\dot{u}_{n+1} + \dot{u}_{n-1} - 2\dot{u}_n) + k_2(z_n - u_n) \\ m_1\ddot{y}_n &= -F_N(t), \quad m_2\ddot{z}_n = -k_2(z_n - u_n) + F_N(t). \end{aligned} \tag{1}$$

Here, u_n, y_n, and z_n denote the barycenter displacements of m_0, m_1, and m_2 in the n^{th} cell, respectively. Denoting $p = y - z$, the piecewise-defined function $F_N(t)$ for the clearance nonlinearity can be fitted with a smooth equation $k_1p + k_Np^n$, where k_1 (k_N) denotes the linear (nonlinear) stiffness coefficient. We specify $F_N(t) = k_1p + k_Np^3$ in theories for generality. Natural frequencies of individual oscillators are $\omega_i = 2\pi f_i = i = 0, 1, 2$. If necessary, the damping coefficient $c_0 = d_0k_0$ in the primary oscillator is considered. The damping mainly comes from the friction between m_0 and the guide rail in experiments. Parameters in simulations and experiments are: $m_0 = 5.8$, $m_1 = 2.1$, $m_2 = 2\,g$; $f_0 = 322$, $f_1 = 100$, and $f_2 = 390.6$ Hz. We take $k_N = 1 \times 10^{13}\,\mathrm{N/m^3}$ to show the nonlinear phenomena in theory.

Moreover, we fabricate a linear metamaterial prototype to establish the controlled experiment for comparison. This controlled sample removes the sphere in the metacell to eliminate nonlinearity, so it is a diatomic model.

The nonlinear strength for the cubic nonlinear system is $\sigma = 3k_NA_0^2/k_1$. The value $\sigma = 32.6$ for $A_0 = 30\,\mu$m shows that we reach enhanced nonlinearity for amplitudes approximate the clearance δ_0. In nonlinear case, the coupling between LR1 and LR2 has been visually defined as the bridging coupling [40]. In experiments, the transmission spectrum, $H(f)$, of a single cell is measured by inputting different levels of white noises, as illustrated in Fig. 1(d). By increasing the excitation, the first resonance notably shifts upwards at first, and the two resonances ultimately merge into a single resonance near 270 Hz. This tremendous shift evidences the enhanced nonlinearity generated by the collisions.

A plane wave in a generic one-dimensional (1D) periodic medium evolves as a function of time, t, and propagation

distance, x:

$$u(x,t) = Ae^{i(\kappa_r x-\omega t)}, \quad A(x) = A_0 e^{-\kappa_I x}, \tag{2}$$

where A_0 is the source amplitude; the wave number $\kappa = \kappa_r + i\kappa_I$, and $\mu = \kappa a = \mu_r + i\mu_I$. The dispersion equation of this NAM is

$$\cos\mu = 1 - \frac{m_0\omega^2}{2k_0} - \frac{\omega^2\omega_2^2\left[m_1\omega_{1eL}^2 + m_2\left(\omega_{1eL}^2 - \omega^2\right)\right]}{2k_0\left[m_2\left(\omega^2 - \omega_{1eL}^2\right)\left(\omega^2 - \omega_2^2\right) - m_1\omega^2\omega_{1eL}^2\right]}, \tag{3}$$

where ω_{1eL} denotes the equivalent natural frequency of m_1 that associates with the equivalent stiffness k_{1eL}. When considering damping, we replace k_0 in Eq. (3) by $k_0(1 + i\omega d_0)$. The bandgap can be described by $|\kappa_I = \mu_I/a| > 0$ solved with Eq. (3).

For linear models, $\omega_{1eL} = \omega_1$. We propose an equivalent linearized approach based on the bifurcation to solve ω_{1eL} for nonlinear models. By specifying $u_n = A\sin\omega t$, $y_n = Y\sin\omega t$, $p_n = P\sin\omega t$ in Eq. (1), neglecting the damping effect and adopting the first-order harmonic balance approach, one can solve the locally resonant responses by the algebraic equations

$$\omega^2 m_1 Y = k_1 P + 3k_N P^3/4$$
$$(k_2 - \omega^2 m_2)(Y - P) - \omega^2 m_1 Y = k_2 A, \tag{4}$$

where Y and P denote the amplitudes of $y(t)$ and $p(t)$, respectively. By specifying A in Eq. (4), the curve, P/A, generates a saddle-node bifurcation near each resonance, as shown with the dark blue circles in Fig. 1(c). ω_{J1} is the first bifurcation frequency (the big red circle). At the bifurcation point, $P = P_{J1}$. The point (ω_{J1}, P_{J1}) is on the response curve of the equivalent linear model (the dashed red curve), where the equivalent stiffness of m_1 becomes k_{1eL}. Therefore,

$$k_{1eL} = k_1 P_{J1} + 3k_N P_{J1}^3/4, \quad \omega_{1eL} = \sqrt{k_{1eL}/m_1}. \tag{5}$$

As ω_{1eL} depends on A, the band structure is determined by the wave amplitude A.

Also, we establish a large numerical model consisting of 500 triatomic cells, as shown in Fig. 1(f). An optimized perfect match layer is connected to its terminal. The incident wave $u_0(t)$ is launched from the other end. This model is available for all frequencies. Furthermore, to separate the incident and reflected waves in the NAM, a linear phononic crystal consisting of 240 primary oscillators is connected to the left terminal of the metamaterial. This linear crystal plays a "buffer" role. It should be noted that the second model is only available for frequencies much lower than the band-gap frequency of the linear phononic crystal, since otherwise the incident wave is reflected by it. We confirm that the results solved with the two models are approximately equal for $f <$ 400 Hz here.

In simulations, 15 periods of standard sinusoidal wave packets are adopted as input sources, $u_0(t) = A_0\sin\omega t$, $\omega = 2\pi f$. The numerical integration approach is adopted to solve responses of the model. Wave transmission at the coordinate x for f is $T(x,f) = A_{av}(x,f)/A_0(f)$, where A_{av} denotes the average value of all peaks of $u(t)$ in the 15 periods with appropriate time decay. At the n^{th} cell in the chain, $T_{(n)}(f_e) = T(x = na, f_e)$.

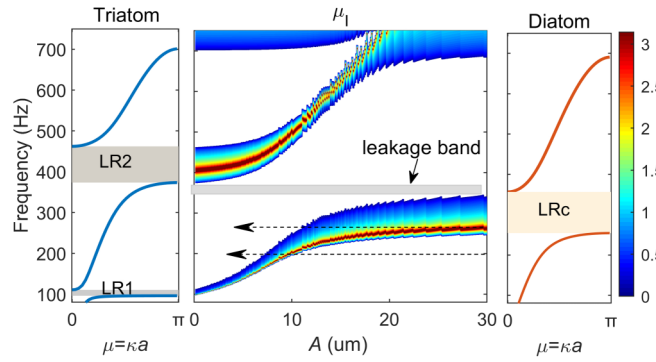

FIG. 2. Amplitude-dependent bandgap. The first and third insets are dispersion curves of the triatomic and diatomic LAMs. The second shading image is the distribution of the imaginary wave vector, $\mu_I = \kappa_I a$, in which the white regions represent $\mu_I = 0$ for passbands. Two dashed arrows represent two cases: the combination (A_0, ω) in bandgap and passband.

III. ACOUSTICAL LIMITING AND ADAPTIVE BANDWIDTH

The amplitude-dependent bandgap is illustrated in Fig. 2. For the linear AM (LAM) with $k_N = 0$, there is a Bragg bandgap (from 700 Hz on) and two LR bandgaps, LR1 and LR2. Their ranges are LR1 (96.1, 110.4) Hz, with a generalized width $\gamma_1 = 0.15$, and LR2 (373.4, 462) Hz, with $\gamma_2 = 0.24$. Thus, LR1 and LR2 are narrow bandgaps (see the Appendix). Moreover, if $k_1 \to \infty$, the triatomic AM degenerates to a diatomic AM characterized by a bandgap LRc (254.4, 356.4) Hz near $f_c = \sqrt{k_2/m_c}/2\pi = 272.8$ Hz thus between LR1 and LR2, $m_c = m_1 + m_2$, $m_c/m_0 = 0.7$, $\gamma = 0.4$.

The amplitude-dependent regime in Fig. 2 shows that the band structure approaches the state of the diatomic LAM if enhanced nonlinearity is generated when A is large. If A decreases from a large value, LRc approaches LR1, and LR2 first decouples from the Bragg gap and then shifts to lower frequencies. A narrow band referred as *leakage band* is never swept by bandgaps. The far-field wave amplitude and transmission are illustrated as functions of A_0 in Figs. 3(a) and 3(b). Frequencies 180, 200, 270, and 600 Hz represent waves in the passbands of the triatomic LAM, and 350 and 400 Hz represent waves in the bandgap LR2.

As shown in Fig. 3(c), for an infinite LAM without damping, we note that $T(x)$ in the bandgaps just gets an finite value about 0.1 rather than a tiny value (e.g., 10^{-4}) even in the far field $n > 80$, because the simulations are performed in time domain and there are always small responses. Moreover, $T(x) \approx 1$ in passbands in theory, and it is independent of propagation distance. In contrast, the amplitude-dependent band structure will present great influences on wave propagations in NAMs.

Properties in passbands are introduced first. For small A_0, the far-field wave amplitude increases linearly with A_0, so $T(x) = 1$. However, after a critical amplitude $A_0 > A_{0c}$, the transmitted amplitude remains constant and even decreases

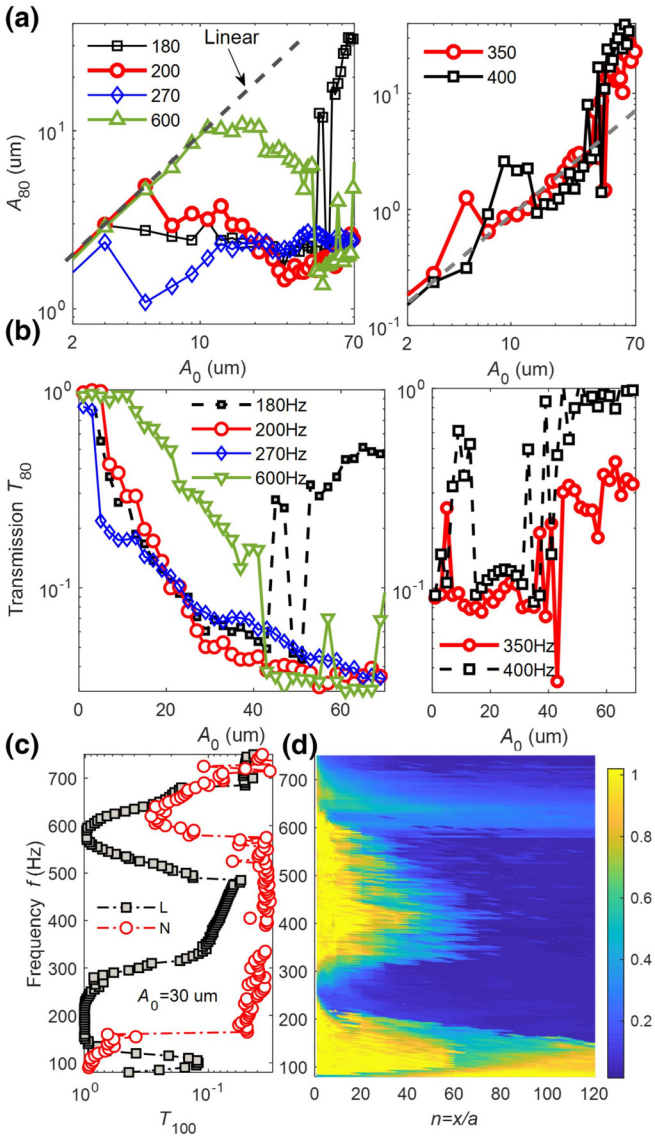

FIG. 3. Acoustical limiting and adaptive bandwidth of NAM. (a),(b) Wave amplitude and transmission at the 80th metacell as functions of A_0 under representative frequencies. (c) Transmissions at the 100th cell, T_{100}. Herein, Land N symbolize the linear and nonlinear cases, respectively. (d) Wave transmission $T(x = na, f)$ at different points along the model of fixed length. $A_0 = 30\,\mu$m in (c), (d).

as A_0 increases, which means the responses are saturated. Therefore, their transmissions decrease as A_0 increases. T_{80} for 200 and 270 Hz reduce to 0.03 at $A_0 = 50\,\mu$m, which is even smaller than that inside the linear bandgaps.

For waves far from LRc (180 Hz here), the wave amplitudes or transmission at a specified distance may fluctuate or increase for large A_0, but they will decrease at a longer propagation distance.

In our NAM, the low-amplitude acoustic/elastic waves can transmit through the material without attenuation, but the large-amplitude waves are suppressed or attenuated. We notice that this phenomenon is analogous with the optical limiting in nonlinear optical materials. Therefore, it is appropriate to refer to the phenomenon as acoustical limiting. Acoustical limiting presents an amplitude-dependent filter. It is not only promising in protecting targets from high-intensity waves like blast and shock waves, as what has been realized in laser technologies, but also in innovating new elements for reduction or isolation of noise/vibration in our everyday life.

For waves inside the bandgaps of LAM (350 and 400 Hz here), the transmission fluctuates with increasing A_0. For large A_0, $T = 1$, indicating that the bandgap becomes a passband according to the amplitude-dependent band structure shown in Fig. 2. Fortunately, the NAM still keeps the ability to limit wave in LR2 in certain amplitude ranges.

Particularly, the acoustical limiting effect of our NAM is ultralow frequency and ultrabroadband. As shown Fig. 3(c), it is surprising that the far-field transmission of the NAM is greatly reduced ($T_{100} \approx 0.03$) in the multioctave range 160–580 Hz. Its generalized bandwidth reaches $\gamma = 2.63$, a double-ultra bandwidth for acoustical limiting. We note that if the wave reduction in this band becomes as large as that in linear bandgaps, one could refer this band as bandgap; but in general, we denote it as a *limiting band*. However, present studies of nonlinear acoustics fail to reveal the mechanisms for these phenomena.

The evolving process for the double-ultra acoustical limiting is depicted in Fig. 3(d). For large incident amplitudes, the near-field ($x < 20a$) attenuating range is not LR1 or LR2. Instead, it is LRc, indicating that m_1 and m_2 in the near-field metacells behave as an integrated resonator, m_c, due to enhanced nonlinearity. Moreover, as x increases, the initial frequency for the greatly attenuated band, denoted f_{st}, shifts downwards gradually, and the transmission above LRc decreases much faster. Thus, the total band for wave attenuation broadens until the entire range from LR1 to LR2 (even all above LR1) obtains great reduction. In other words, we cumulate the gap effect in Fig. 2 from the incident source to the deep inside the NAM. This process shows that the limiting band in this NAM adaptively evolving from a narrow one, LRc, into a double-ultra one covering the range LR1–LR2, $\gamma = 3.5$ (at least), which far exceeds the bandwidth of the LAM with $m_c/m_0 = 0.7$. We term this phenomenon a *self-broadening* or *adaptive-broadening*: The bandwidth self-adapts to the propagation distance. As the propagation distance depends on the propagation time, a space-dependent property is also time-dependent. It is also different from the tunable bandgap by changing the incident amplitude, A_0, in nonlinear crystals. Here, the variable is propagation distance or time. Actually, adaptive broadening highlights a concept of band structure that is closely related to the limiting and self-action mechanisms.

IV. MECHANISMS

This section presents the mechanisms for the acoustical limiting and its self-broadening band. According to Eq. (2), the amplitude reduction in propagation distance $\Delta x = a\Delta n$ denotes $e^{-\kappa_1 \Delta x} = e^{-\mu_1 \Delta n}$. Bandgaps lead to great attenuation in short Δx caused by the large μ_1, i.e., $\mu_1 \gg 0$. This is the attenuation process of evanescent waves (see the Appendix). As the bandgap is amplitude dependent, the process for generating the limiting effect depends on the combination

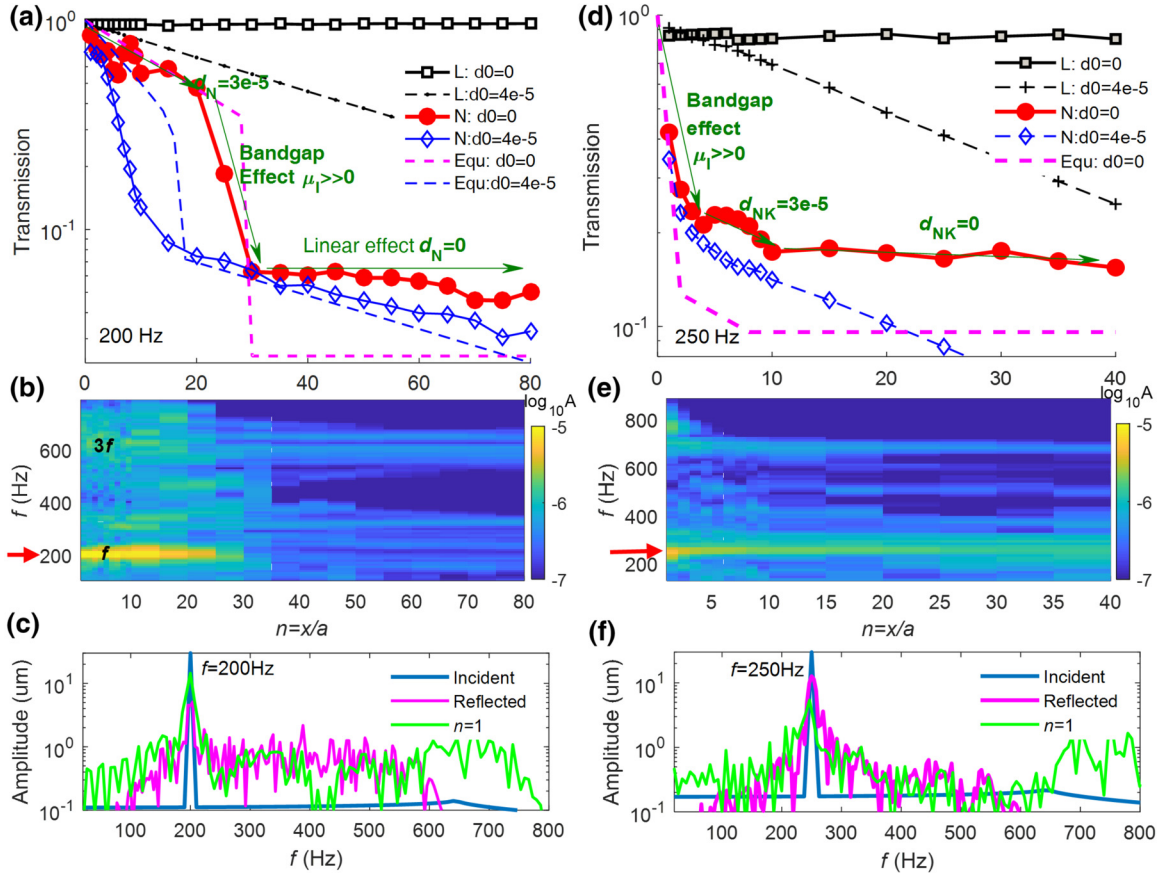

FIG. 4. Mechanisms for acoustical limiting in the NAM. (a), (b), (c) Results for 200 Hz. (d), (e), (f) Results for 250 Hz. (a), (d) Transmissions in different cases vary as functions of propagation distance $n = x/a$. Herein, L and N in legends symbolize the numerical results of the linear and nonlinear model, respectively; Equ represents the results solved by the equivalent theory. $d0 = 0$ and $d0 = 4e\text{-}5$ mean the damping coefficient $d_0 = 0$ and $d_0 = 4 \times 10^{-5}$ s, respectively. In (d), we use $0.55\kappa_I$ in the equivalent theory due to its approximate nature of the nonlinear model. (b), (e) Spectra of the displacement $u_n(t)$ for increasing n. (c), (f) Displacement spectra of the input wave, reflected wave and waves at the first triatomic cell ($n = 1$), respectively. Damping is not considered in (b), (c), (e), (f). All numerical results are solved with the model containing the linear phononic crystal "buffer" shown in Fig. 1(f).

parameters of incident, (A_0, ω). There are mainly two cases: the combination (A_0, ω) locates either in (i) the passbands of LAM, or (ii) in the bandgap LRc shown in Fig. 2. Two representative frequencies, 200 and 250 Hz, are taken to show the attenuation processes for cases (i) and (ii), respectively. $A_0 = 30\,\mu$m is specifically chosen here. The main difference between the two cases lies in the position for generating the band-gap effect (see the Appendix). Results are illustrated in Fig. 4.

If (A_0, ω) first appears in the passbands, there are three steps in the nonlinear attenuation process. In linear regimes, $\kappa_I = 0$ for $d_0 = 0$, thereby $T(x) = 1$, the reflection is 0, and the band structure never varies. In contrast, the wave spectra in Figs. 4(b) and 4(c) indicate that waves in NAM undergo harmonic generation [37] (mainly third harmonic due to cubic nonlinearity) and chaotic responses that pump the fundamental energy to a broad spectral band. The narrow-band input becomes a broadband wave featuring a continuous spectrum. These processes reduce the total amplitude. Defining κ_N as the entire attenuation rate induced by them, we have $A(x) = A_0 e^{-\kappa_N x} e^{-\kappa_I x}$. Simulations and experiments indicate that $\kappa_N \propto \omega$. We adopt $\kappa_N = d_N \omega$ to approximate this effect. As shown by the dashed arrows in Fig. 2, the reduction of $A(\mathrm{x})$ shifts the bandgaps downwards. When the combination (A, ω) appears in the bandgap at a critical position, a significant reduction (more than an order of magnitude) of evanescent waves can be induced within just $3 \sim 10$ cells because $\max(\mu_I) > 3$ and average $(\mu_I) > 0.5$ here. For the case shown in Fig. 4(a), the fast reduction appears in the position range $20 < n < 30$. Here, the band-gap effect occurs inside the material and quite far from the "surface". As waves inside a NAM are a superposition of the forward transmitted and backward reflected waves, the nontransmitted energy now spectrally broad is actually reflected by the NAM [see Fig. 4(c)]. Eventually, as shown in Fig. 4(b), for small $A(\mathrm{x})$ in far-field metacells, nonlinearity is weak and the linearity plays a dominant role, so $d_N = 0$ and LR1, LR2, and Bragg bandgaps are active to reflect broadband energy in the chaotic wave. However, the residual energy in passbands can still propagate without attenuation. Thus, the far-field transmission in the self-broadening limiting band may be greater than that in the LAM bandgap. As depicted in Fig. 4(a), by specifying $d_N = 3 \times 10^{-5}\,\mathrm{s\,m^{-1}rad^{-1}}$, the analytical transmission derived from the equivalent theory agrees very well with the numerical curve for $d_0 = 0$, confirming that the acoustical limiting effect mainly arises from the moving band-gap effect.

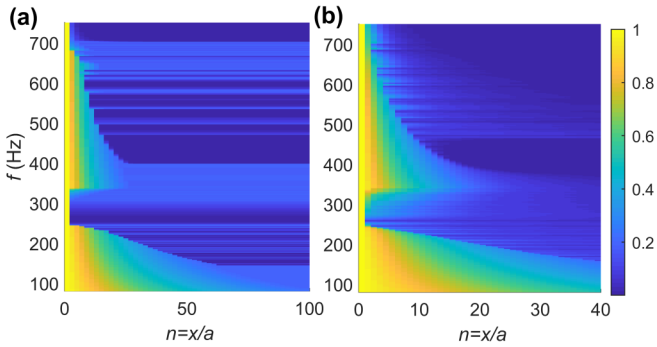

FIG. 5. Transmission $T(x = na, f)$ solved with the equivalent method, $d_N = 3 \times 10^{-5}\,\mathrm{s\,m^{-1}rad^{-1}}$, $A_0 = 30\,\mu\mathrm{m}$. (a) $d_0 = 0$; (b) Damped case for $d_0 = 4 \times 10^{-5}$ s.

If (A_0, ω) first appears in LRc, as shown in Fig. 4(f), most input energy is reflected by several metacells near the incident boundary, thereby the amplitude decreases rapidly [see Fig. 4(d)]. The transmission at the fourth cell is as low as 0.2. Then, harmonic generation and chaotic response diminish the amplitude slowly. If the third harmonic falls in the Bragg bandgap above 700 Hz (here $3f = 750$ Hz), it will diminish within short propagation distance [see Fig. 4(d)]. At last, linearity plays a dominant role in the aforementioned process when the amplitude becomes small. The second step for chaotic responses may not happen if the reduction in the first step directly leads the AM into the linear regime. Considering the approximate nature of the equivalent theory, it still reproduces the numerical trends, which confirms again that the moving band-gap effect is the main source for transmission reduction.

The analyses above clarify that (i) The acoustical limiting in this NAM mainly arises from the band-gap effect; (ii) The ultrabroad limiting bandwidth is induced by the adaptive-broadening band-gap effect; (iii) Harmonic generation and chaotic response are key mechanisms to initiate adaptive broadening.

As shown Fig. 5(a), transmissions $T(x, f)$ solved with the equivalent method are in accordance with Fig. 3(d). These analyses indicate that the position (inside NAM), where the band-gap effect happens, depends on A_0 and frequency. Inversely, the initial and cut-off frequencies of the bandgap vary with position, i.e., the band structure is space-amplitude-dependent rather than only amplitude dependent. It is a self-strengthening process: Once the wave attenuation begins, band structure varies and broader ranges are swept by bandgaps, then more energy is reflected. Therefore, the attenuation bandwidth adaptively broadens as propagation distance increases, and an ultrabroad limiting band is eventually observed. Of particular significance is the fact that this "adaptive band" is essentially different from the conventional "invariant band" or "tunable band by changing amplitude". The adaptive property indicates that the Bloch theorem is incompatible with enhanced nonlinearity, where the spatial and temporal variations have to be considered.

However, if (A_0, ω) first appears in passbands, a great transmission loss induced by the band-gap effect requires a long propagation distance as d_N is small. Higher A_0 needs longer distance (i.e., material thickness) before reaching the zone of quick reduction where the band-gap effect occurs. Accelerating the self-broadening needs a greater decay rate. Fortunately, material damping is unavoidable in practice and it can exhibit a positive role here. As shown in Figs. 4(a) and 4(d), the wave amplitude in linear metamaterials decays exponentially as the propagation distance increases when $d_0 \neq 0$ in Eq. (1). By introducing a weak damping, $d_0 = 4 \times 10^{-5}$ s, in the numerical model and equivalent theory, the critical distance for obtaining the band-gap effect is greatly shortened. The equivalent result still reproduces the shorten critical distance. For example, $n = 5$ for the wave (30 μm, 200 Hz) now. Therefore, the self-broadening can be accelerated by the presence of weak material damping in practice. By comparing the linear and nonlinear cases for $d_0 = 4 \times 10^{-5}$ s in Figs. 4(a) and 4(d), we note that the acoustical limiting effect in NAM still mainly derives from the band-gap effect but not the weak damping. A clear evidence is that their decaying ratios are like those observed for $n > 15$ (where linearity plays a dominant role) but the amplitude of LAM is $5 \sim 10$ times larger. The amplitude difference derives from the band-gap effect.

V. EXPERIMENTAL DEMONSTRATIONS

Different experiments were carefully established to demonstrate the limiting effect, its band-gap mechanisms, and adaptive-broadening bandwidth. As shown in Fig. 1(e), the transient velocity responses, $V_n(t)$, of the primary oscillators are synchronously measured by three laser Doppler vibrometers, $V_n(t) \approx 2\pi f A_n(t)$. By trying to use different incident wave forms, we find that adding a slowly rising edge and a slowly trailing edge, expressed as $A_0 \sin(\omega t/10) \sin\omega t$, at both ends of the standard sinusoidal wave packet can eliminate the transient impact responses of the exciter (see the Supplemental material [42]). Both the maximum and average peak values of the propagation packet are extracted to calculate the wave transmission, and we confirm that trends shown by them are consistent.

A. Controlled experiment

First, we establish a controlled experiment on the diatomic linear metamaterial prototype whose oscillators m_2 are removed to eliminate the influences of nonlinearity. Experimental and numerical transmissions at different propagation distances are shown in Fig. 6. Comparing the incident amplitude used in Fig. 8(a) below, the amplitude $A_0(f)$ adopted in the controlled experiment is high enough to observe the nonlinear phenomena, if there was nonlinearity. The desired great wave attenuation appears in the locally resonant bandgap near 400 Hz. However, no acoustical limiting effect is observed below the bandgap. Small attenuation in this sample results from the damping. Moreover, by comparing the numerical and experimental transmissions at different positions we obtain that the damping coefficient is $d_0 = (2.5 \pm 2) \times 10^{-5}$ s in experiments.

B. Demonstrations of acoustical limiting and bandgap effect

Second, we measure the influences of A_0 on the transmissions of the NAM at different positions, as shown in

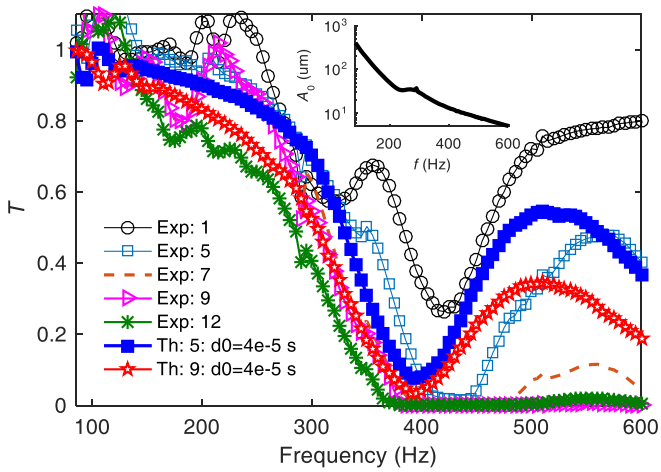

FIG. 6. Experimental and theoretical transmissions of the controlled linear metamaterial model. In legends, "Exp" represents the experimental results; "Th" denotes the numerical results; the number, j, represents the transmission at the j^{th} cell. For example, "Exp: 5" denotes the experimental transmission at the fifth cell. The smaller inset shows the A_0 spectral amplitude from 80 to 600 Hz.

Fig. 7. Moreover, to reproduce the experimental phenomena, we establish a numerical model consisting of 30 cells containing clearance nonlinearity. The clearance $\delta_0 = 40\,\mu$m and a weak damping $d_0 = 1 \times 10^{-5}$ s are specifically chosen in this model. As shown in Fig. 7(c), the experimental and numerical transmissions are perfectly agreeing, which confirms the validity of experiments again.

For waves below 370 Hz, the transmissions decrease with increasing A_0. The low-amplitude wave can propagate, but the large-amplitude waves are greatly attenuated. For example, $T_8 < 0.1$ for $A_0 = 50\,\mu$m. Therefore, an unambiguous acoustical limiting effect is observed. For high-frequency waves (600 Hz here), Fig. 6 shows that damping has larger influence, and the maximum A_0 is limited by the power of the vibration exciter in experiment, but a nascent acoustical limiting effect is also observed at the fifth cell for $A_0 > 30\,\mu$m. Moreover, T_5 for 250 Hz starts to increase for $A_0 > 100\,\mu$m. For incident waves inside the bandgap LR2 (400 Hz here), small waves are suppressed but the large amplitude wave can propagate through eight metacells with small attenuation. These trends agree well with those in Fig. 3(b).

Then, we address the proof by contradiction to demonstrate that the band-gap effect rather than the damping is the key mechanism for the acoustical limiting. As is well known, damping effect for high-frequency waves is greater than for low-frequency waves, though the damping is very weak, as confirmed in Fig. 6. Therefore, if the wave attenuation mainly arose from the damping, the attenuation rates of 250 and 270 Hz should be always smaller than the rate of 600 Hz. However, the attenuation processes in Fig. 7(c) largely manifest the opposite situation. The waves at 250 and 270 Hz undergo great reduction within three metacells near the source, and then their amplitudes decrease more slowly than waves at 600 Hz. This process is identical to the attenuation of evanescent wave in the bandgap shown in Fig. 4(d), and it is confirmed by the numerical curves in Fig. 7(c). Therefore, this

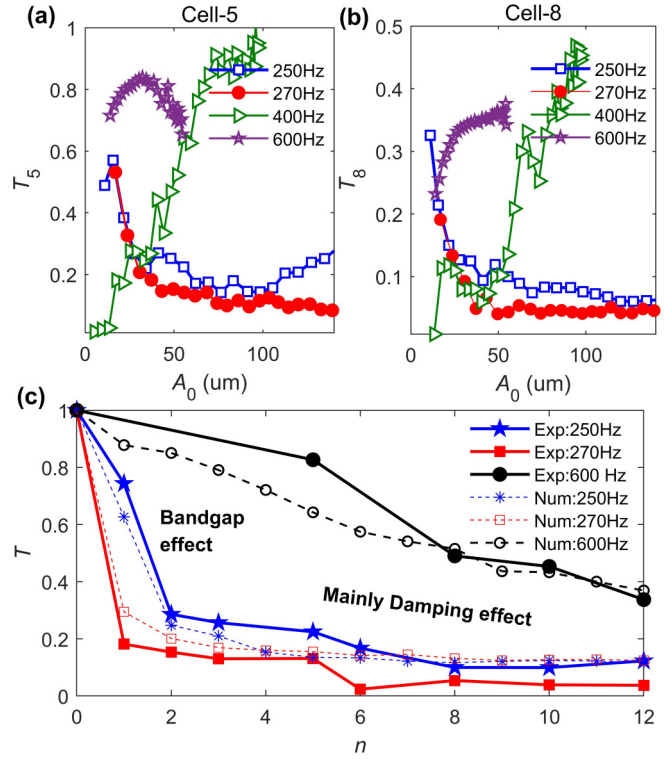

FIG. 7. Acoustical limiting in experiments. (a), (b) Transmissions at the fifth and eighth cell change as functions of A_0. (c) Attenuation processes of representative waves for $A_0 = 50\,\mu$m. Herein, Exp represents the experimental results. Num represents the numerical results calculated with the model containing clearance-nonlinearity. $\delta_0 = 40\,\mu$m and $d_0 = 1 \times 10^{-5}$ s in the model.

experiment demonstrates that the acoustical limiting is mainly induced by the band-gap effect.

C. Demonstration of adaptive bandwidth

Eventually, we demonstrate the adaptive bandwidth for acoustical limiting, as shown in Fig. 8. NAM responses under three driving levels, 2, 4, and 8 V, are measured. A_0 decreases with f in the experiments [Fig. 8(a)]. If the incident packets of level 8 V are directly input into the numerical model containing clearance-nonlinearity, Fig. 8(c) shows that the experimental and numerical transmissions are approximately equal. Moreover, the near-field transmission exhibits quite an abrupt jump at a frequency, f_{B} (420 Hz in this case). By observing the relative motions in the first cell [Fig. 8(b)], we find that f_{B} is the grazing bifurcation [41] frequency of the vibroimpact oscillator. Nonlinearity disappears due to $|p| < \delta_0$ for $f > f_{\text{B}}$.

At a certain propagation distance, a greater transmission loss in 200–350 Hz is induced by a larger A_0 [Fig. 8(d)] due to acoustic limiting. Figures 8(e) and 8(f) indicates that the near-field ($n < 3$) transmission near 273 Hz is greatly reduced, but waves in 0–255 Hz and 350 Hz-f_{B} can still propagate. This confirms that the near-field NAM behaves as a quasilinear diatomic model that leads to the attenuation in LRc. This is in accordance with the trends in Figs. 7(c) and 3(d). As the propagation distance/time increases, waves in the near-field

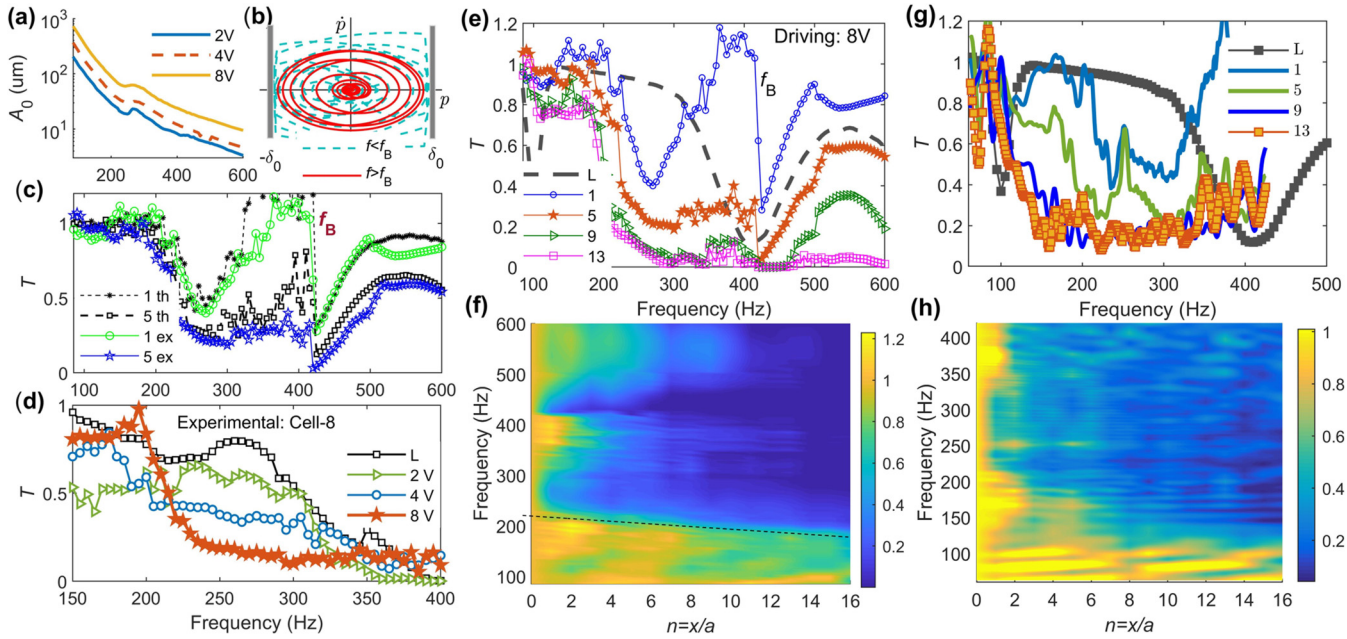

FIG. 8. Experimental demonstration. Panels (a)–(f) are results for inputting sinusoidal packets. (a) Driving amplitude A_0. (b) Phase diagrams for numerical responses of cell 1 immediately before the bifurcation frequency f_B, $f < f_B$, and immediately after f_B, $f > f_B$. $\dot{p} = dp/dt$. (c) Experimental, ex, and theoretical, th, transmissions at cell 1 and cell 5 under the same input, level 8 V. (d) Experimentally measured transmissions at the eighth cell. Here, 2, 4, and 8 V are the three driving levels for the NAM; L represents the result for the diatomic LAM prototype. (e), (f) Transmissions under 8 V. (g), (h) Transmissions obtained in sweep-frequency experiments. In (c), (e), (g), the number, n, in legends represents the n^{th} cell; L represents the numerical result of the fifth cell in the linearized model. (f), (h) Transmission $T(x = na, f_e)$, $n = x/a$.

passbands, 200 Hz-f_B, are attenuated gradually due to the shifting bandgap. The entire limiting band becomes broader at longer propagation distances, successfully demonstrating the spatial and temporal adaptive band structure and adaptive-broadening bandwidth. The limiting band at the 13$^{\text{th}}$ cell has reached 200–500 Hz for levels 8 V (it is 180–500 Hz for level 4 V [42]).

Moreover, this experiment still proves that opening the bandgap by observing the residual amplitude below 180 Hz requires a longer propagation distance, which is attributed to the challenge in attenuating all broadband energy of packets. The fast sweep-frequency experiment [Figs. 8(g) and 8(h)] shows a faster self-broadening speed, especially for $f <$ 250 Hz. Herein the band-gap successfully expands to 130 Hz at the 13th cell, which is close to LR1. Certain weak peaks at high frequencies correspond to the standing waves arising from the boundary reflection of the finite NAM. Images of Figs. 8(f) 8(h) also agree with the equivalent analytical image show in Fig. 5.

These experiments demonstrate that the bandgap can adaptively expand to at least $130 \sim 500$ Hz ($\gamma = 2.85$) within $9 \sim 13$ cells. Comparing with the linear metamaterial with $m_c/m_0 = 0.7$, the unusual double-ultralimiting band extends far beyond the limitation dictated by mass ratio of a conventional LR bandgap.

VI. CONCLUSIONS AND DISCUSSIONS

This paper introduces a NAM containing enhanced nonlinear interaction. We present the theoretical and experimental demonstrations of the efficient and broadband acoustical limiting effect in nonlinear acoustic/elastic media, and we report that the band-gap effect can adaptively broaden as the propagation distance/time increases. Of particular relevance is that the adaptive-broadening band-gap effect dominates the broadband acoustical limiting. The limiting efficiency can reach 97%. The self-action occurs because the band structure is distance-amplitude-dependent inside the NAM rather than only amplitude dependent. As clarified, harmonic generation and chaotic responses play key roles in initializing the adaptive process, and weak damping can somehow counterintuitively accelerate the broadening speed. In experiments, an ultrabroad acoustical limiting band (also the band-gap effect) is performed within a short propagation distance, which overcomes the limitation of the mass ratio for conventional locally resonant bandgaps in linear metamaterials.

The limiting band here is different from the chaotic passband because the broadband resonance attenuations in chaotic passbands originate from the chaotic vibrations but not the adaptive band-gap effect [38,39]. Although a triatomic NAM is considered here, we anticipate that the self-broadening bandgap occurs in NAMs containing enhanced nonlinearly coupled oscillators, for example, diatomic NAMs. Actually, a crystal (no matter phononic or photonic) whose bandgaps can be greatly shifted by amplitude could possess this adaptive property. Here, we state two easily satisfied preconditions for self-broadening: The material is "monocrystal" and the spatial distribution of its nonlinear coefficient is uniform. In a nonlinear metamaterial, "monocrystal" means the metacells along the wave propagation path are same. The uniform

nonlinear coefficient in this paper means the parameter k_N in every unit cell is same; in nonlinear optics, it means the n^{th}-order electric susceptibilities at different positions inside the crystal are same.

The two fundamental principles provide the first step towards extensive potential applications in innovating devices for protecting targets from high-intensity elastic waves, for wave isolation, and for self-modulating waves. Moreover, it will be interesting to extend this line of study to higher dimensions (2D and 3D). Due to the analogous properties of elastic, optical, and electromagnetic waves, expanding the scope of the self-broadening bandgap is also desirable. Therefore, we expect that our study will be of interest for the broader wave physics community.

ACKNOWLEDGMENTS

This research was funded by the National Natural Science Foundation of China (Projects No. 11872371, No. 11991032, and No. 11991034). Moreover, we especially thank Prof. B. Li and Reviewers for providing excellent suggestions.

APPENDIX: DEFINITIONS OF CONCEPTS

1. Bandgap effect

The amplitude reduction in a bandgap depends on the accumulated exponential decay in a certain propagation distance, $\exp(-\kappa_I \Delta x)$. Here, the band-gap effect means the wave attenuation due to $\kappa_I > 0$ in the undamped case, but the accumulating distance Δx is not considered. In our NAM, the Δx may be short in some cases. Therefore, the amplitude reduction range is directly defined as limiting band instead of bandgap.

2. Generalized width of a bandgap

The generalized width of a bandgap is $\gamma = (f_{cut} - f_{st})/f_{st}$, where $f_{st}(f_{cut})$ is its initial (cutoff) frequency. A LAM's LR bandgap obeys the law $\gamma \approx \sqrt{1 + m_c/m_0} - 1$, where m_c (m_0) denotes the mass of the local resonator and primary oscillator. A smaller mass ratio m_c/m_0 is better for most applications. For example, $\gamma \approx 0.3$ for $m_c/m_0 = 0.7$, and a huge value, $m_c/m_0 = 3$, is required to obtain $\gamma = 1$ in LAM. Therefore, $\gamma > 1$ can be regarded as a double-ultra bandgap because there is $\gamma << 1$ generally.

3. Piecewise nonlinear functions

In experiments, the nonlinear force $F_N(t)$ generated by the contact between the sphere and the hollow cylinder is

$$F_N(t) = \begin{cases} k_1 p_n & \text{for} \quad |p_n| \leqslant \delta_0 \\ k_1 p_n + A_c (p_n - \delta_0)^{3/2} & \text{for} \quad p_n > \delta_0 \\ -k_1 p_n - A_c (-p_n - \delta_0)^{3/2} & \text{for} \quad p_n < -\delta_0 \end{cases}. \tag{A1}$$

Here, δ_0 denotes the width of the clearance and $A_c = 2E_s\sqrt{r_s}/[3(1-\nu^2)]$, where E_s and υ represent the elastic modulus and Poisson's ratio of the softer medium, respectively. Here, $E_s = 70\,\text{GPa}$, $\upsilon = 0.3$. The piecewise function $F_N(t)$ described by Eq. (8) can be fitted with a smooth equation $k_1 p + k_N p^n$. The linear coefficient, k_1, is constant but the nonlinear coefficient, k_N, depends on the clearance, δ_0. By fitting the curve, we obtain $k_N = \alpha \delta_0^{-n}$ and $\alpha = 0.3$ for $\delta_0 = 45\,\mu$m, so $k_N \approx 3.3 \times 10^{12}\,\text{N/m}^3$ for cubic nonlinearity.

4. Nonlinear strength

The nonlinear strength $\sigma < 0.1$ is weak nonlinearity and $\sigma = 0.3$ can generate strongly nonlinear phenomena [19]. In our experiments, if we approximate the clearance nonlinearity with the smooth cubic nonlinearity, we obtain $k_N = 3.3 \times 10^{12}\,\text{N/m}^3$. The amplitude under 8 V reaches 533 and 53 μm for 100 and 300 Hz, respectively, and their $\sigma = 3392$ and 33.5. They are huge numbers relative to $\sigma = 0.3$. Therefore, it can generate enhanced nonlinear responses.

5. Evanescent wave

The evanescent wave intensity decays exponentially (rather than sinusoidally) with distance, x, from the interface at which they are formed according to $E = E_0 e^{-\gamma x}$, where γ is the attenuation coefficient and E_0 is the initial intensity.

[1] J. Kim, S. S. Baik, S. H. Ryu, Y. Sohn, S. Park, B. G. Park, J. Denlinger, Y. Yi, H. J. Choi, and K. S. Kim, Science **349**, 723 (2015).
[2] M. Abdi-Jalebi, Z. Andaji-Garmaroudi, S. Cacovich, C. Stavrakas, B. Philippe, J. M. Richter, M. Alsari, E. P. Booker, E. M. Hutter, A. J. Pearson, S. Lilliu, T. J. Savenije, H. Rensmo, G. Divitini, and C. Ducati *et al.*, Nature (London) **555**, 497 (2018).
[3] N. Li, J. Ren, L. Wang, G. Zhang, P. Hänggi, and B. Li, Rev. Mod. Phys. **84**, 1045 (2012).
[4] Y. Kivshar, Natl. Sci. Rev. **5**, 144 (2018).
[5] G. S. He and S. H. Liu, *Physics of Nonlinear Optics* (World Scientific, Singapore, 1999).
[6] E. Makri, T. Kottos, and I. Vitebskiy, Phys. Rev. A **91**, 043838 (2015).
[7] Y. S. Tamgadge, A. L. Sunatkari, S. S. Talwatkar, V. G. Pahurkar, and G. G. Muley, Opt. Mater. **51**, 175 (2016).
[8] L. W. Tutt and T. F. Boggess, Prog. Quant. Electron. **17**, 299 (1993).
[9] S. Guddala and S. A. Ramakrishna, Opt. Lett. **41**, 5150 (2016).
[10] H. R. Seren, J. Zhang, G. R. Keiser, S. J. Maddox, X. Zhao, K. Fan, S. R. Bank, X. Zhang, and R. D. Averitt, Light Sci. Appl. **5**, e16078 (2016).
[11] J. Balapanuru, J. X. Yang, S. Xiao, Q. Bao, M. Jahan, L. Polavarapu, J. Wei, Q. H. Xu, and K. P. Loh, Angew. Chem. Int. Ed. Engl. **49**, 6549 (2010).
[12] M. Maldovan, Nature (London) **503**, 209 (2013).
[13] M. Schwarze, W. Tress, B. Beyer, F. Gao, R. Scholz, C. Poelking, K. Ortstein, A. A. Gunther, D. Kasemann, D. Andrienko, and K. Leo, Science **352**, 1446 (2016).

[14] Z. Chen, X. Zhang, S. Lin, L. Chen, and Y. Pei, National Sci. Rev. **5**, 888 (2018).
[15] R. Bogue, Sens. Rev. **37**, 305 (2017).
[16] V. Laude, Y. Achaoui, S. Benchabane, and A. Khelif, Phys. Rev. B **80**, 092301 (2009).
[17] B. Shi, W. Cai, X. Zhang, Y. Xiang, Y. Zhan, J. Geng, M. Ren, and J. Xu, Sci. Rep. **6**, 26796 (2016).
[18] J. J. Bonnefois, G. Guida, A. Priou, M. Nevière, and E. Popov, J. Opt. Soc. Am. A **23**, 842 (2006).
[19] X. Fang, J. Wen, J. Yin, D. Yu, and Y. Xiao, Phys. Rev. E **94**, 052206 (2016).
[20] W. Jiao and S. Gonella, Phys. Rev. E **99**, 042206 (2019).
[21] J. Zhou, L. Dou, K. Wang, D. Xu, and H. Ouyang, Nonlinear Dyn. **96**, 647 (2019).
[22] T. F. Khalkhali, R. Shiri, H. Shahrokhabadi, and A. Bananej, Indian J. Phys. **93**, 1537 (2019).
[23] M. Flammini, G. Di Domenico, D. Pierangeli, F. Di Mei, A. J. Agranat, and E. DelRe, Phys. Rev. A **98**, 033808 (2018).
[24] Y. Y. Chen, M. V. Barnhart, J. K. Chen, G. K. Hu, C. T. Sun, and G. L. Huang, Compos. Struct. **136**, 358 (2016).
[25] J. Y. Tsao, S. Chowdhury, M. A. Hollis, D. Jena, N. M. Johnson, K. A. Jones, R. J. Kaplar, S. Rajan, C. G. Van de Walle, E. Bellotti, C. L. Chua, R. Collazo, M. E. Coltrin, J. A. Cooper, and K. R. Evans *et al.*, Adv. Electron. Mater. **4**, 1600501 (2018).
[26] Z. Liu, X. Zhang, Y. Mao, Y. Y. Zhu, Z. Yang, C. T. Chan, and P. Sheng, Science **289**, 1734 (2000).
[27] S. Zhang, C. Xia, and N. Fang, Phys. Rev. Lett. **106**, 024301 (2011).
[28] H. Abbaszadeh, A. Souslov, J. Paulose, H. Schomerus, and V. Vitelli, Phys. Rev. Lett. **119**, 195502 (2017).
[29] N. Kaina, F. Lemoult, M. Fink, and G. Lerosey, Nature (London) **525**, 77 (2015).
[30] M. Yang and P. Sheng, Annu. Rev. Mater. Res. **47**, 83 (2017).
[31] V. Romero-García, A. Krynkin, L. M. Garcia-Raffi, O. Umnova, and J. V. Sánchez-Pérez, J. Sound Vib. **332**, 184 (2013).
[32] G. Ma and P. Sheng, Sci. Adv. **2**, e1501595 (2016).
[33] Y. Li, J. Lan, B. Li, X. Liu, and J. Zhang, J. Appl. Phys. **120**, 145105 (2016).
[34] X. Fang, J. Wen, J. Yin, and D. Yu, AIP Adv. **6**, 121706 (2016).
[35] V. F. Nesterenko, C. Daraio, E. B. Herbold, and S. Jin, Phys. Rev. Lett. **95**, 158702 (2005).
[36] G. Wehmeyer, T. Yabuki, C. Monachon, J. Wu, and C. Dames, Appl. Phys. Rev. **4**, 041304 (2017).
[37] X. Fang, J. Wen, D. Yu, G. Huang, and J. Yin, New J. Phys. **20**, 123028 (2018).
[38] X. Fang, J. Wen, B. Bonello, J. Yin, and D. Yu, Nat. Commun. **8**, 1288 (2017).
[39] X. Fang, J. Wen, B. Bonello, J. Yin, and D. Yu, New J. Phys. **19**, 053007 (2017).
[40] X. Fang, J. Wen, D. Yu, and J. Yin, Phys. Rev. Appl. **10**, 054049 (2018).
[41] M. di Bernardo, C. J. Budd, A. R. Champneys, P. Kowalczyk, A. B. Nordmark, G. O. Tost, and P. T. Piiroinen, SIAM Rev. **50**, 629 (2008).
[42] See Supplemental Material at http://link.aps.org/supplemental/10.1103/PhysRevB.101.104304 for details on the numerical models, simulations, and experiments.